

Meson spectroscopy of exotic symmetries of Ising criticality in Rydberg atom arrays

Joseph Vovrosh ^{1,*} Julius de Hond ¹ Sergi Julià-Farré ¹ Johannes Knolle ^{2,3,4} and Alexandre Dauphin ^{1,†}

¹PASQAL SAS, 24 rue Emile Baudot - 91120 Palaiseau, Paris, France

²Technical University of Munich, TUM School of Natural Sciences,

Physics Department, TQM, 85748 Garching, Germany

³Munich Center for Quantum Science and Technology (MCQST), Schellingstr. 4, 80799 München, Germany

⁴Blackett Laboratory, Imperial College London, London SW7 2AZ, United Kingdom

The Ising model serves as a canonical platform for exploring emergent symmetry in quantum critical systems. The critical point of the 1D Ising chain is described by a conformal Ising field theory, which remains integrable in the presence of a magnetic perturbation leading to massive particles associated with the exceptional Lie algebra E_8 . Coupling two Ising chains in a ladder leads to an even richer $\mathcal{D}_8^{(1)}$ symmetry. Experimental signatures of the associated particle excitations have arguably been observed in scattering studies of the spin chain material CoNb_2O_6 . Here, we probe these emergent symmetries in a Rydberg atom quantum processing unit, leveraging its tunable geometry to realize both chain and ladder configurations. We identify mass spectra consistent with E_8 and $\mathcal{D}_8^{(1)}$ symmetries at the respective critical points. Our results demonstrate the power of Rydberg platforms for investigating symmetry emergence in quantum many-body systems and provide a direct window into the interplay of confinement, geometry and criticality.

Introduction - Emergent symmetries at quantum critical points offer profound insights into the universal behavior of many-body systems [1]. Among these, the exceptional Lie algebra E_8 has garnered significant attention because it emerges at the quantum critical point of the basic one-dimensional (1D) transverse field Ising chain (TFIC) when subjected to a longitudinal field [1, 2]. Instead of a quantum critical continuum response, discrete peaks of bound states appear in the structure factor, signatures of which have been experimentally observed in the quasi-1D Ising ferromagnet CoNb_2O_6 [3]. Remarkably, the spectrum of bound states have universal energy ratios dictated by the E_8 symmetry given in Fig. 1(a).

However, subsequent studies have indicated that the excitation spectrum of CoNb_2O_6 may be more accurately described by the affine Lie algebra $\mathcal{D}_8^{(1)}$ [4–6], arising from strong interchain interactions [see Fig. 1(a)] that effectively render the system as an Ising ladder rather than a simple chain. This shift in symmetry underscores the sensitivity of emergent phenomena to the underlying geometry and interactions within the system.

The bound states emerging at perturbed quantum critical points are intimately related to the phenomenon of confinement, i.e. deep in the ordered phase perturbations lead to a monotonically increasing potential between domain-wall quasi-particles and the formation of discrete mesonic bound states [7, 8]. The latter then continuously connect to the discrete particles of the critical points and govern the real-time quench dynamics [9, 10]. In quantum Ising chains confinement can be induced through various mechanisms, including external magnetic fields [10, 11], long-range interactions [12, 13] and interchain couplings [14, 15], leading to rich excitation spectra that reflect the system’s symmetry properties [9].

In this work, we utilize the versatility of Rydberg atom arrays to experimentally investigate the emergence of E_8 and $\mathcal{D}_8^{(1)}$ symmetries in 1D Ising chains and Ising ladders, respectively [16–18]. By precisely engineering the geometry and interactions within these quantum simulators, we are able to probe the critical points of these systems and observe the corresponding bound state spectra. Previously, signatures of confinement have been reported in analogue [13] and digital Quantum Processing Units (QPU) [11, 19] for isolated Ising chains away from their critical points. Here, our spectroscopic measurements and new ladder geometry reveal characteristic frequencies that align with the predictions of the E_8 and $\mathcal{D}_8^{(1)}$ theories, providing compelling evidence for these emergent symmetries of the underlying critical points. Our study demonstrates the power of QPUs in the analog mode in exploring complex many-body physics and paves the way for future investigations into higher-dimensional systems and other exotic symmetries.

Confinement in Ising Chains - Throughout this work, we consider the transverse field Ising model, which describes interacting spin- $\frac{1}{2}$ particles

$$H_I = -J \sum_{i,j} \sigma_i^z \sigma_j^z - h_x \sum_i \sigma_i^x, \quad (1)$$

where σ_i^α are the usual Pauli matrix operators acting on the i^{th} site, J is the spin-spin interaction, and h_x is the transverse field. In the rest of the work, we set $J = 1$.

In a one-dimensional TFIC quasiparticle excitations of this Hamiltonian correspond to free fermions. By considering $h_x < h_c$, where $h_c = 1$ is the critical point of the Hamiltonian, quasiparticles are well approximated by simple domain walls. Introducing a finite longitudinal field, $-h_z \sum_i \sigma_i^z$, two quasiparticles experience a linear confining force proportional to both their separation and h_z [7], see Fig. 1(b). Consequently, each pair of quasiparticles form a mesonic bound state with a mass defined

* joseph.vovrosh@pasqal.com

† alexandre.dauphin@pasqal.com

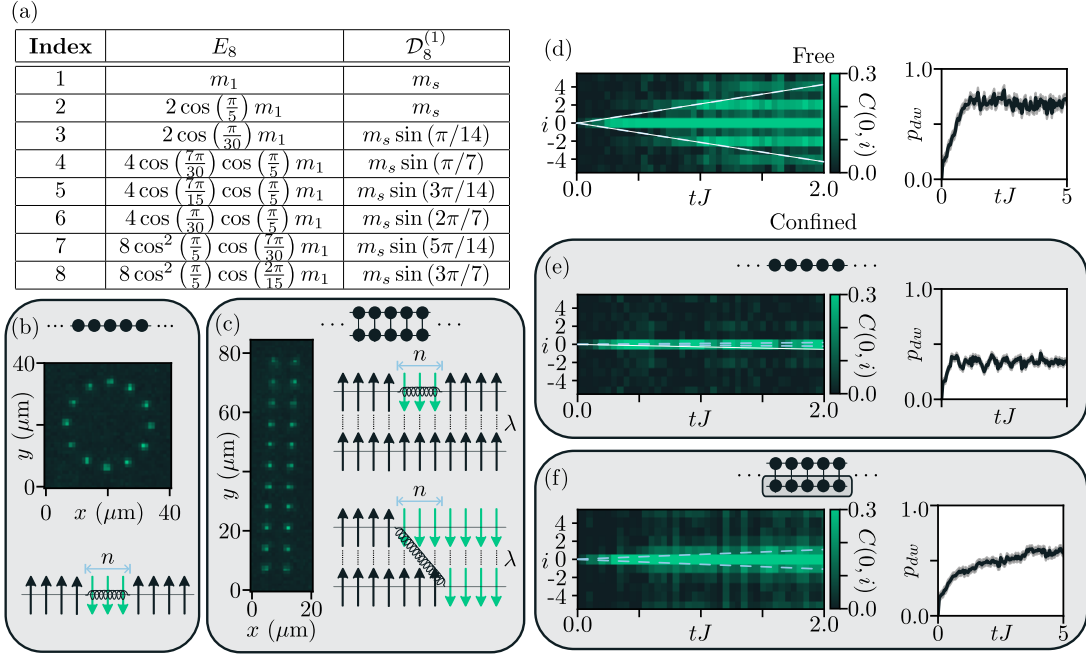


FIG. 1: (a) Meson masses predicted by the E_8 and \mathcal{D}_8 symmetries [2, 4]. (b-c) The atomic registers realised in the neutral atom platform to study both the 1D Ising chain and quasi-1D Ising ladder respectively, as well as schematics of the corresponding domain wall meson excitations. (d-f) QPU data for an Ising Chain (d) with $N = 12$, $h_x = 1$ and $h_z = 0$, (e) and in the presence of a longitudinal field $h_z = 4$. Figure (f) depicts weakly coupled Ising ladders with $N = 11$, $h_z = 0$ and $\lambda = 1$. The left panel of each (d-f) shows the correlation spreading in the Ising model after a quench from the $|00 \dots 00\rangle$ state (with theoretical predictions in dashed blue) and each right panel shows the number of domain walls after this quench, normalised by the number of nearest neighbor pairs.

by $m_i = E_i - E_0$ where E_i is the i^{th} energy level (with zero momentum). Confinement is known to slow correlation and entanglement spread [11], delay thermalisation [12, 20] and lead to interesting phenomena such as string breaking [21] and inelastic collisions [19, 22–25].

Confinement is also known to occur in the weakly coupled Transverse Field Ising Ladder (TFIL) for $h_x < h_c$, and *without* the need for an additional magnetic field,

$$H = H_I^1 + H_I^2 - \lambda \sum_i \sigma_{1,i}^z \sigma_{2,i}^z, \quad (2)$$

in which H_I acts on the i^{th} chain, $i \in \{1, 2\}$, and $\lambda \ll 1$. In this regime, pairs of excitations also experience a linear confining force, this time proportional to their separation and to the interchain coupling, λ . Recent theoretical studies employing time-dependent density matrix renormalization group methods have revealed that the excitation spectrum of the TFIL exhibits a rich structure of bound states [14]. These include both *intra* and *interchain* mesonic excitations, as well as bound states of mesons themselves, see Fig. 1(b). The presence of these higher-order bound states indicates a hierarchical confinement mechanism unique to the ladder geometry described by two coupled Ising conformal field theories [4].

Although the quantum field theory predictions associated with both the E_8 and $\mathcal{D}_8^{(1)}$ symmetries for these models are derived assuming only nearest-neighbor interactions for both the TFIC with a longitudinal field

and TFIL, the E_8 symmetry remains approximately preserved even in the presence of long-range interaction tails and other erroneous terms, such as those encountered in trapped-ion systems [26] and additional subdominant terms required for more precise models of CoNb_2O_6 [9]. In the following sections, we extend this perspective to show that the $\mathcal{D}_8^{(1)}$ symmetry is robust against long-range interactions, such as those realized in Rydberg arrays.

Experimental Considerations - An Ising-type Hamiltonian can be naturally realised with arrays of neutral atoms in optical tweezers. When excited to high-lying Rydberg states, they exhibit large dipolar interactions. By defining the atomic ground state as $|0\rangle$ and the Rydberg state as $|1\rangle$, the Hamiltonian can be expressed as

$$H_{\text{Ryd}} = \sum_{i,j>i} \frac{C_6}{|\mathbf{r}_i - \mathbf{r}_j|^6} n_i n_j + \frac{\hbar\Omega(t)}{2} \sum_i \sigma_i^x - \sum_i \frac{\hbar\delta_i(t)}{2} \sigma_i^z, \quad (3)$$

where $n_i = (1 + \sigma_i^z)/2$, $C_6 > 0$ is the strength of the Van der Waals antiferromagnetic interaction, and $\Omega(t)$ and $\delta(t)$ are the Rabi frequency and detuning induced by the external laser [27]. By adjusting both the Rabi frequency and detuning, one can map this Hamiltonian to an Ising model exactly for systems with periodic boundary conditions (PBC), and up to a local longitudinal field at the edge of the system for open boundary conditions (OBC), full details can be found in App. A. Furthermore, we can also probe the dynamics of the ferromagnetic Ising model for initial states preserving time-reversal symmetry [28].

In particular, a TFIC with a longitudinal field can thus be realised in a Rydberg atom platform through arranging atoms in a 1D chain, or in our case, a circular geometry allowing for the consideration of PBC, see Fig. 1(b). Furthermore, we realize the TFIL in our Rydberg atom platform through arranging atoms in two 1D chains. Note, given a two-dimensional (2D) trapping region, it is not possible to exactly realise an Ising ladder with PBC and thus throughout this work we consider OBC for this quasi-1D system, see Fig. 1(b).

Observations of Confinement - A quintessential signature of confinement dynamics is the suppression of correlation spreading following a sudden quench, that is $C(i, j) = \langle \sigma_i^z \sigma_j^z \rangle - \langle \sigma_i^z \rangle \langle \sigma_j^z \rangle$. In conventional critical systems, correlations typically spread ballistically, governed by the maximal group velocity of quasiparticles, for the TFIC this is given by $\mathcal{V} = 2 \min(1, h_x)$ [10, 29, 30]. However, in confined systems, the presence of an effective potential between quasiparticles significantly slows down their propagation, leading to a characteristic suppression of entanglement growth and a deviation from the expected light-cone dynamics. This behavior has been extensively studied in both theoretical models [10, 12, 14] and experimental platforms [11, 13, 31], making it a key observable for identifying confinement effects.

In our experiments, we directly observe the effect of confinement by comparing different regimes. In the absence of confinement, correlations spread with a clear light-cone, consistent with the Lieb-Robinson bound [30], which governs the maximum speed of information propagation in quantum systems, see Fig. 1(d). However, in the presence of a longitudinal field, or for weakly coupled Ising chains, the spreading of correlations is significantly slowed, see Fig. 1(e-f). This behavior aligns with theoretical predictions for confined systems, where the effective meson velocity, calculated through the maximal group velocity of the low lying energy level (see App. B), governs the dynamics of correlation spreading [10, 11].

Beyond slowing the spread of correlations, we also observe that confinement suppresses the growth in the number of domain walls, a hallmark of constrained dynamics, see Fig. 1(e-f) right panels. This suppression is consistent with the picture of meson-like bound states limiting the available phase space for domain wall proliferation. These results provide direct experimental evidence of confinement-induced slowdown in both correlation spreading and excitation dynamics—a qualitative feature also observed in quantum simulations of confined lattice gauge theories in one [32] and two dimensions [33].

Observation of Symmetries - To study the emergent E_8 and $\mathcal{D}_8^{(1)}$ symmetries at the critical points of the Ising chain and ladder, we first optimize the atomic register, Rabi frequency, and detuning to ensure that the systems under investigation accurately reflect the theoretically predicted energy spectra. In order to verify the presence of an E_8 symmetry, we examine a 12-qubit Ising chain with PBC. By tuning the Rabi frequency and detuning such that $h_x = 1$ and $h_z = 4$ we obtain the resulting

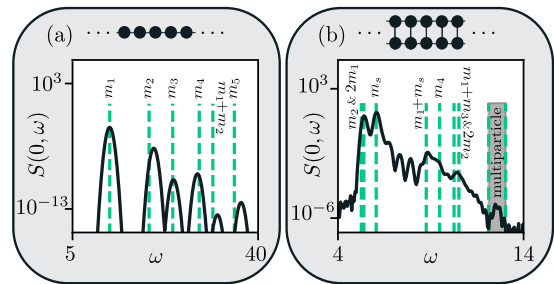


FIG. 2: Zero-momentum dynamical structure factor for (a) the TFIC with a longitudinal field with $h_x = 1$ and $h_z = 4$, and (b) the TFIL with $h_x = 1$, $h_z = 0$, and inter-chain coupling $\lambda = 1$. In both cases, vertical dashed lines indicate the theoretically predicted mass ratios associated with emergent symmetries: E_8 in the chain and $\mathcal{D}_8^{(1)}$ in the ladder.

zero-momentum dynamical structure factor $S(k = 0, \omega)$ (DSF) from the full eigenspectrum obtained via exact diagonalisation, as shown in Fig. 2(a). The ratios of the peaks seen in these results closely match the theoretical predictions for E_8 symmetry [9]. Note, that despite the relatively small length of the chain the lowest masses follow the prediction because the strong longitudinal field suppresses finite size effects [26].

Similarly, to assess whether the Rydberg ladder is well described by the $\mathcal{D}_8^{(1)}$ symmetry, we consider two 11-qubit Ising chains with OBC. The atomic separation, Rabi frequency, and detuning are adjusted such that $\lambda = 1$, $h_x = 1$, and $h_z = 0$, with a total of 22 qubits. We simulate the DSF with the help of matrix product state methods [9]. As shown in Fig. 2(b), the peaks in $S(k = 0, \omega)$ align well with the predicted peaks for the $\mathcal{D}_8^{(1)}$ symmetry [5, 6].

For both emergent symmetries, E_8 and $\mathcal{D}_8^{(1)}$, we extract meson spectra through a two-step approach: first via classical simulation of quench dynamics to establish a baseline, and subsequently on the QPU. The classical simulations allow us to compute exact long-time dynamics and verify that the chosen protocol faithfully encodes the meson masses in the time-domain evolution. By performing a Fourier transform of the simulated observables, we obtain a clear spectral decomposition with dominant frequencies, ω_i , that match linear combinations of the theoretically predicted meson mass ratios shown with vertical dashed lines in Fig. 3(a-b) [34].

To replicate this protocol on the QPU, we must account for the device's limited coherence time by restricting the accessible evolution window. Although the QPU simulation times are limited to $tJ \sim 5$, these surpass significantly those achievable in previous works [13, 34, 35], enabling meaningful exploration of the dynamics. For the TFIC with a longitudinal field, the meson spectrum spans a wide energy range, so we select a relatively large longitudinal field, $h_z = 4$, to compress the relevant frequencies into a shorter timescale that fits within the quantum hardware's operational regime. However, this large field

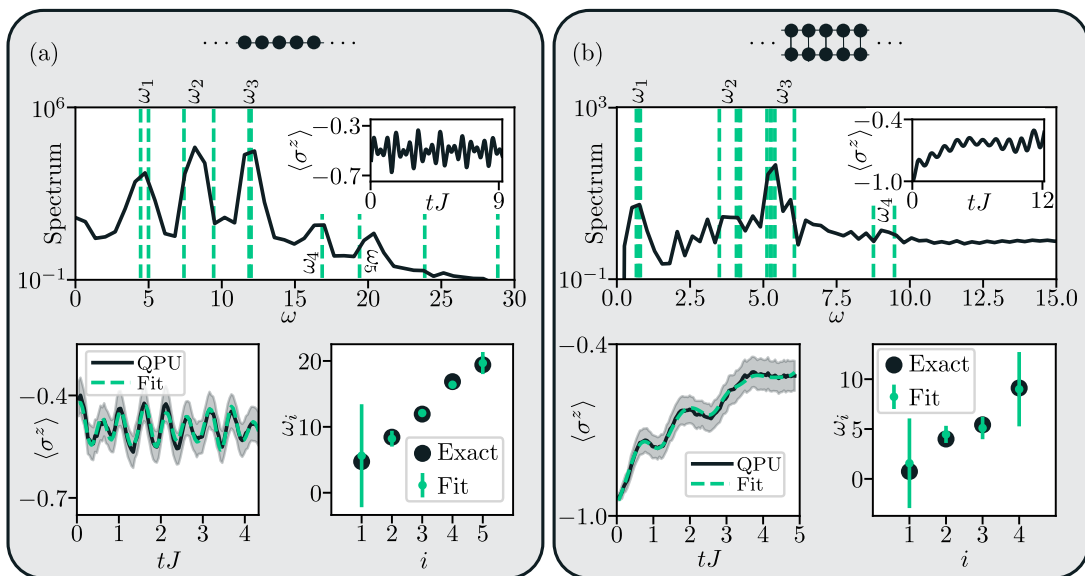


FIG. 3: Analysis of quench dynamics performed on from the $|00\dots 0\rangle$ state to both the TFIC with a longitudinal field with (a) $N = 12$, $h_x = 1$ and $h_z = 4$ and (b) the TFIL with $N = 11$, $h_x = 1$, $h_z = 0$ and $\lambda = 1$. The upper panels shows the Fourier analysis of a quench, performed with classical methods, with real-time data in inset. The dominant peaks, corresponding to the meson masses predicted by E_8 and $\mathcal{D}_8^{(1)}$ symmetry - and their differences - are indicated by vertical dashed lines. The lower panels show the non-equilibrium experimental results from a quench.

A Fourier series ansatz is fitted to the data and used to extract the dominant frequencies.

causes the trivial initial state $|0\rangle^{\otimes N}$ to primarily couple to the lowest masses m_1 and m_2 of the E_8 spectrum, severely limiting the visibility of higher meson states. To address this, we employ a two-stage quench protocol: the system is first evolved with $h_x = 1$ and $h_z = 0$ for a short time ($tJ \approx 0.5$), generating an intermediate state with nontrivial structure. We then perform a sudden quench to $h_x = 1$ and $h_z = 4$, initiating dynamics from this state with an enhanced overlap with multiple E_8 meson eigenstates. This thus yields a richer frequency spectrum.

In contrast, for the $\mathcal{D}_8^{(1)}$ case realized in the TFIL geometry, the ground state $|0\rangle^{\otimes 2N}$ naturally overlaps with several meson modes. As such, a single quench from this initial state is sufficient to excite a broad spectrum of meson masses, eliminating the need for a preparatory evolution stage. Hence we consider a single quench from $|0\rangle^{\otimes N}$ to the TFIL with $h_x = 1$ and $\lambda = 1$.

To quantitatively analyze the QPU data, we fit the resulting time traces to a multi-frequency Fourier ansatz, with the same number of dominant frequencies, ω_i as in the classical simulations, using the ADAM optimizer [36]. We run 20 independent fits over 20,000 epochs each to ensure convergence and robustness (see App. C). The extracted frequencies are then averaged across fits, and the results are shown in Fig. 3 (lower panel). Despite the presence of statistical fluctuations and hardware-induced noise, the mean values agree well with the predictions ω_i . The agreement to classical simulations thus confirms that the QPU captures the key spectral signatures associated with both E_8 and $\mathcal{D}_8^{(1)}$ symmetry. We stress that the confinement mechanism for the two cases is quite distinct because the TFIL does not need a longitudinal field,

but rather the other chain acts as a dynamical confining field captured in our ladder geometry. For a study of the noise seen in the QPU results, see App. D.

Conclusion and Outlook - In this paper, we observed qualitatively and quantitatively emergent symmetries of Ising models at criticality with the help of a neutral atom QPU. We first probed confinement for both a 1D Ising chain with PBC and an Ising ladder with OBC by taking advantage of the flexibility of the atomic register. In particular, we observed the slow down of correlation spread due to confinement in these models. Finally, by performing meson spectroscopy, we showed that the emergent E_8 and $\mathcal{D}_8^{(1)}$ symmetries in these models can be extracted from the real time quench dynamics. Our QPU therefore allows us to probe in particular the low energy spectrum of the magnetic material CoNb_2O_6 and we found a qualitative agreement with neutron scattering observations.

While all the dynamics simulated on the QPU in this work are classically tractable for the system sizes and dimensions considered, neutral atom QPUs can be scaled to hundreds of atoms in 2D. In fact, some studies have already studied the physics of confinement in 2D systems with neutral atom platforms [37], as well as superconducting qubits [33]. With improved initial state preparation, meson scattering experiments [19, 22–24] will be possible and will allow for a better characterization of the elastic or inelastic nature of the scattering.

Finally, neutral atom QPUs can readily be used to probe Hilbert Space Fragmentation [38]. The latter has been observed in 1D neutral atom platforms [39, 40] and going to 2D promises a much richer phenomenology. It is known that accurately simulating the dynamics of 2D

models near criticality is exponentially costly in memory and computation time [41, 42] and therefore the QPUs can shed a new light allow to quantum criticality in 2D.

ACKNOWLEDGMENTS

A.D. thanks Christophe Jurczak for a careful reading of the manuscript. J.K. thanks the hospitality of the Aspen Center for Physics, which is supported by National Science Foundation grant PHY-2210452. J.K. acknowledges support from the Deutsche Forschungsge-

meinschaft (DFG, German Research Foundation) under Germany's Excellence Strategy– EXC–2111–390814868 and DFG Grants No. KN1254/1-2, KN1254/2-1 and TRR 360 - 492547816, as well as the Munich Quantum Valley, which is supported by the Bavarian state government with funds from the Hightech Agenda Bayern Plus. J.K. further acknowledges support from the Imperial-TUM flagship partnership. Pasqal's team acknowledges funding from the European Union the projects EQUALITY (Grant Agreement 101080142) and PASQuanS2.1 (HORIZON-CL4-2022-QUANTUM02-SGA, Grant Agreement 101113690).

-
- [1] G. Mussardo, *Statistical field theory: an introduction to exactly solved models in statistical physics* (Oxford University Press, USA, 2010).
- [2] A. B. Zamolodchikov, Integrals of motion and S-matrix of the (scaled) $T = T_c$ Ising model with magnetic field, *International Journal of Modern Physics A* **4**, 4235 (1989).
- [3] R. Coldea, D. A. Tennant, E. M. Wheeler, E. Wawrzynska, D. Prabhakaran, M. Telling, K. Habicht, P. Smeibidl, and K. Kiefer, Quantum criticality in an Ising chain: Experimental evidence for emergent E_8 symmetry, *Science* **327**, 177–180 (2010).
- [4] A. LeClair, A. Ludwig, and G. Mussardo, Integrability of coupled conformal field theories, *Nuclear Physics B* **512**, 523–542 (1998).
- [5] Y. Gao, X. Wang, N. Xi, Y. Jiang, R. Yu, and J. Wu, Spin dynamics and dark particle in a weak-coupled quantum Ising ladder with $\mathcal{D}_8^{(1)}$ spectrum (2024), arXiv:2402.11229 [cond-mat.str-el].
- [6] N. Xi, X. Wang, Y. Gao, Y. Jiang, R. Yu, and J. Wu, Emergent $\mathcal{D}_8^{(1)}$ spectrum and topological soliton excitation in CoNb_2O_6 (2024), arXiv:2403.10785 [cond-mat.str-el].
- [7] S. B. Rutkevich, Energy spectrum of bound-spinons in the quantum Ising spin-chain ferromagnet, *Journal of Statistical Physics* **131**, 917–939 (2008).
- [8] J. Greensite, *An introduction to the confinement problem*, Vol. 821 (Springer, 2011).
- [9] J. A. Kjäll, F. Pollmann, and J. E. Moore, Bound states and E_8 symmetry effects in perturbed quantum Ising chains, *Physical Review B* **83**, 10.1103/physrevb.83.020407 (2011).
- [10] M. Kormos, M. Collura, G. Takács, and P. Calabrese, Real-time confinement following a quantum quench to a non-integrable model, *Nature Physics* **13**, 246–249 (2016).
- [11] J. Vovrosh and J. Knolle, Confinement and entanglement dynamics on a digital quantum computer, *Scientific Reports* **11**, 10.1038/s41598-021-90849-5 (2021).
- [12] F. Liu, R. Lundgren, P. Titum, G. Pagano, J. Zhang, C. Monroe, and A. V. Gorshkov, Confined quasiparticle dynamics in long-range interacting quantum spin chains, *Physical Review Letters* **122**, 10.1103/physrevlett.122.150601 (2019).
- [13] W. L. Tan, P. Becker, F. Liu, G. Pagano, K. S. Collins, A. De, L. Feng, H. B. Kaplan, A. Kyprianidis, R. Lundgren, W. Morong, S. Whitsitt, A. V. Gorshkov, and C. Monroe, Domain-wall confinement and dynamics in a quantum simulator, *Nature Physics* **17**, 742–747 (2021).
- [14] F. B. Ramos, M. Lencsés, J. C. Xavier, and R. G. Pereira, Confinement and bound states of bound states in a transverse-field two-leg Ising ladder, *Phys. Rev. B* **102**, 014426 (2020).
- [15] G. Lagnese, F. M. Surace, M. Kormos, and P. Calabrese, Confinement in the spectrum of a Heisenberg–Ising spin ladder, *Journal of Statistical Mechanics: Theory and Experiment* **2020**, 093106 (2020).
- [16] A. Browaeys and T. Lahaye, Many-body physics with individually controlled Rydberg atoms, *Nature Physics* **16**, 132–142 (2020).
- [17] P. Schauss, Quantum simulation of transverse Ising models with Rydberg atoms, *Quantum Science and Technology* **3**, 023001 (2018).
- [18] H. Labuhn, D. Barredo, S. Ravets, S. de Léséleuc, T. Macrì, T. Lahaye, and A. Browaeys, Tunable two-dimensional arrays of single Rydberg atoms for realizing quantum Ising models, *Nature* **534**, 667–670 (2016).
- [19] J. Vovrosh, R. Mukherjee, A. Bastianello, and J. Knolle, Dynamical hadron formation in long-range interacting quantum spin chains, *PRX Quantum* **3**, 10.1103/prxquantum.3.040309 (2022).
- [20] S. Birnkammer, A. Bastianello, and M. Knap, Prethermalization in one-dimensional quantum many-body systems with confinement, *Nature Communications* **13**, 10.1038/s41467-022-35301-6 (2022).
- [21] R. Verdel, F. Liu, S. Whitsitt, A. V. Gorshkov, and M. Heyl, Real-time dynamics of string breaking in quantum spin chains, *Phys. Rev. B* **102**, 014308 (2020).
- [22] P. I. Karpov, G. Y. Zhu, M. P. Heller, and M. Heyl, Spatiotemporal dynamics of particle collisions in quantum spin chains (2020), arXiv:2011.11624 [cond-mat.quant-gas].
- [23] A. Milsted, J. Liu, J. Preskill, and G. Vidal, Collisions of false-vacuum bubble walls in a quantum spin chain, *PRX Quantum* **3**, 10.1103/prxquantum.3.020316 (2022).
- [24] R. G. Jha, A. Milsted, D. Neuenfeld, J. Preskill, and P. Vieira, Real-time scattering in Ising field theory using matrix product states (2024), arXiv:2411.13645 [hep-th].
- [25] J. Schuhmacher, G.-X. Su, J. J. Osborne, A. Gandon, J. C. Halimeh, and I. Tavernelli, Observation of hadron scattering in a lattice gauge theory on a quantum computer (2025), arXiv:2505.20387 [quant-ph].

- [26] J. Knaute and P. Hauke, Relativistic meson spectra on ion-trap quantum simulators, *Phys. Rev. A* **105**, 022616 (2022).
- [27] L. Henriët, L. Beguin, A. Signoles, T. Lahaye, A. Browaeys, G.-O. Reymond, and C. Jurczak, Quantum computing with neutral atoms, *Quantum* **4**, 327 (2020).
- [28] R. Menu, *Gaussian-state approaches to quantum spin systems away from equilibrium*, Ph.D. thesis, Université de Lyon (2020).
- [29] P. Calabrese and J. Cardy, Time Dependence of Correlation Functions Following a Quantum Quench, *Phys. Rev. Lett.* **96**, 136801 (2006).
- [30] E. H. Lieb and D. W. Robinson, The finite group velocity of quantum spin systems, *Commun.Math. Phys.* **28**, 251 (1972).
- [31] M. Kebrič, J. C. Halimeh, U. Schollwöck, and F. Grusdt, Confinement in 1+1d \mathbb{Z}_2 lattice gauge theories at finite temperature (2024), arXiv:2308.08592 [cond-mat.quant-gas].
- [32] J. Mildenerger, W. Mruczkiewicz, J. C. Halimeh, Z. Jiang, and P. Hauke, Confinement in a \mathbb{Z}_2 lattice gauge theory on a quantum computer, *Nature Physics* **21**, 312–317 (2025).
- [33] T. A. Cochran, B. Jobst, E. Rosenberg, Y. D. Lensky, G. Gyawali, N. Eassa, M. Will, D. Abanin, R. Acharya, L. A. Beni, *et al.*, Visualizing dynamics of charges and strings in (2+1)d lattice gauge theories (2024), arXiv:2409.17142 [quant-ph].
- [34] C. Lamb, Y. Tang, R. Davis, and A. Roy, Ising meson spectroscopy on a noisy digital quantum simulator, *Nature Communications* **15**, 10.1038/s41467-024-50206-2 (2024).
- [35] J. Vovrosh, K. E. Khosla, S. Greenaway, C. Self, M. S. Kim, and J. Knolle, Simple mitigation of global depolarizing errors in quantum simulations, *Physical Review E* **104**, 10.1103/physreve.104.035309 (2021).
- [36] D. P. Kingma and J. Ba, Adam: A method for stochastic optimization (2017), arXiv:1412.6980 [cs.LG].
- [37] D. González-Cuadra, M. Hamdan, T. V. Zache, B. Braverman, M. Kornjača, A. Lukin, S. H. Cantú, F. Liu, S.-T. Wang, A. Keesling, M. D. Lukin, P. Zoller, and A. Bylinskii, Observation of string breaking on a (2 + 1)d rydberg quantum simulator, *Nature* **642**, 321–326 (2025).
- [38] A. Yoshinaga, H. Hakoshima, T. Imoto, Y. Matsuzaki, and R. Hamazaki, Emergence of Hilbert space fragmentation in Ising models with a weak transverse field, *Physical Review Letters* **129**, 10.1103/physrevlett.129.090602 (2022).
- [39] L. Zhao, P. R. Datta, W. Tian, M. M. Aliyu, and H. Loh, Observation of quantum thermalization restricted to Hilbert space fragments and F_{2k} scars, *Phys. Rev. X* **15**, 011035 (2025).
- [40] S. Karch, S. Bandyopadhyay, Z.-H. Sun, A. Impertro, S. Huh, I. P. Rodríguez, J. F. Wienand, W. Ketterle, M. Heyl, A. Polkovnikov, *et al.*, Probing quantum many-body dynamics using subsystem loschmidt echos, arXiv preprint arXiv:2501.16995 (2025).
- [41] T. J. Osborne, Hamiltonian complexity, *Rep. Prog. Phys.* **75**, 022001 (2012).
- [42] P. Coleman, *Introduction to Many-Body Physics* (Cambridge University Press, Cambridge, 2015).
- [43] A. Paszke, S. Gross, F. Massa, A. Lerer, J. Bradbury, G. Chanan, T. Killeen, Z. Lin, N. Gimelshein, L. Antiga, A. Desmaison, A. Köpf, E. Yang, Z. DeVito, M. Raison, A. Tejani, S. Chilamkurthy, B. Steiner, L. Fang, J. Bai, and S. Chintala, Pytorch: An imperative style, high-performance deep learning library (2019), arXiv:1912.01703 [cs.LG].
- [44] S. Julià-Farré *et al.*, An exhaustive noise model of a neutral atom quantum processing unit (2025), manuscript in preparation.

Appendix A: Simulating the Ising model with Rydberg atoms

Rydberg atom arrays provide a versatile and highly controllable platform for simulating quantum spin models, including variants of the transverse-field Ising model. In these systems, neutral atoms are trapped in optical tweezers and coherently excited to high-lying Rydberg states, where they experience strong van der Waals interactions. Each atom effectively behaves as a spin-1/2 system, with the computational basis defined by the ground state $|g\rangle$ and a Rydberg state $|r\rangle$. In this work, we employ ^{87}Rb atoms, encoding the states as $|g\rangle = |5S_{1/2}, F = 2, m_F = 2\rangle$ and $|r\rangle = |60S_{1/2}, m_J = 1/2\rangle$. The dynamics of the system are governed by the many-body Hamiltonian

$$H_{\text{Ryd}} = \sum_{i,j>i} \frac{C_6}{|\mathbf{r}_i - \mathbf{r}_j|^6} n_i n_j + \frac{\Omega}{2} \sum_i \sigma_i^x - \frac{\delta}{2} \sum_i \sigma_i^z, \quad (\text{A1})$$

where $n_i = (1 + \sigma_i^z)/2$ is the projector onto the Rydberg state, $|\mathbf{r}_i - \mathbf{r}_j|$ is the interatomic distance, C_6 is the van der Waals interaction coefficient, Ω is the Rabi frequency of the laser driving the $|g\rangle \leftrightarrow |r\rangle$ transition, and δ is the detuning of the laser. By making the mapping

$$J_{ij} = \frac{C_6}{4r_{ij}^6}, \quad h_x = \frac{\Omega}{2}, \quad h_z = \frac{\delta}{2}, \quad (\text{A2})$$

we obtain an effective spin-1/2 Hamiltonian resembling the transverse-field Ising model

$$H_{\text{Ryd}} = \sum_{i,j>i} J_{ij} \sigma_i^z \sigma_j^z + h_x \sum_i \sigma_i^x + h_z \sum_i \sigma_i^z + \sum_i \Delta_i, \quad (\text{A3})$$

such that

$$\Delta_i = \sum_{j>i} J_{ij} (\sigma_i^z + \sigma_j^z). \quad (\text{A4})$$

This erroneous term acts as an effective shift in the longitudinal field. In the bulk of a spin chain or regular lattice, this term can be compensated by a suitable choice of the laser detuning. Although H_{Ryd} features only antiferromagnetic interactions ($J_{ij} > 0$), the dynamics of the ferromagnetic regime can still be explored. Specifically, when the detuning is tuned such that $\delta_i = \sum_j J_{ij}/2$, the dynamics under H_{Ryd} become equivalent (up to a global phase) to those under $-H_{\text{Ryd}}$, provided the initial state respects time-reversal symmetry. In experiments, the Rydberg atom platform allows for site-resolved measurement of spin observables. In particular, the local magnetization $\langle \sigma_i^z \rangle$ and two-point correlations $\langle \sigma_i^z \sigma_j^z \rangle$ can be directly inferred from fluorescence imaging, which provides projective measurements of the atomic populations n_i with single-site resolution.

Appendix B: Meson velocities from DSF results

In Fig. 4, we present the dynamical structure factor for both the *ferromagnetic* transverse-field Ising chain and the transverse-field Ising ladder configurations considered in this work. The dynamical structure factor, which captures the spectral weight of excitations as a function of momentum and energy, reveals key features of the low-energy quasiparticle spectrum. From these spectra, we identify the dispersion relation of the lowest-lying excitations and extract the corresponding energy-momentum relationship, $\epsilon(k)$. The group velocity, defined as $v_g = \partial\epsilon(k)/\partial k$, characterizes the speed at which these quasiparticles propagate through the system. By locating the point at which this derivative is maximized, we determine the maximal group velocity, a key parameter that sets the upper bound for the speed of information and correlation spreading in the confined regime.

From our analysis, we find that the maximal group velocity (in units sites $\times J$) is approximately $v_g \approx 0.1$ for the TFIC with a longitudinal field and significantly larger, $v_g \approx 0.6$, for the TFIL. This difference reflects the varying strength of confinement in the two models, with the more weakly confined TFIL supporting faster, more delocalized quasiparticles. These values are consistent with the observed differences in the spreading of correlations and domain wall dynamics in the main text.

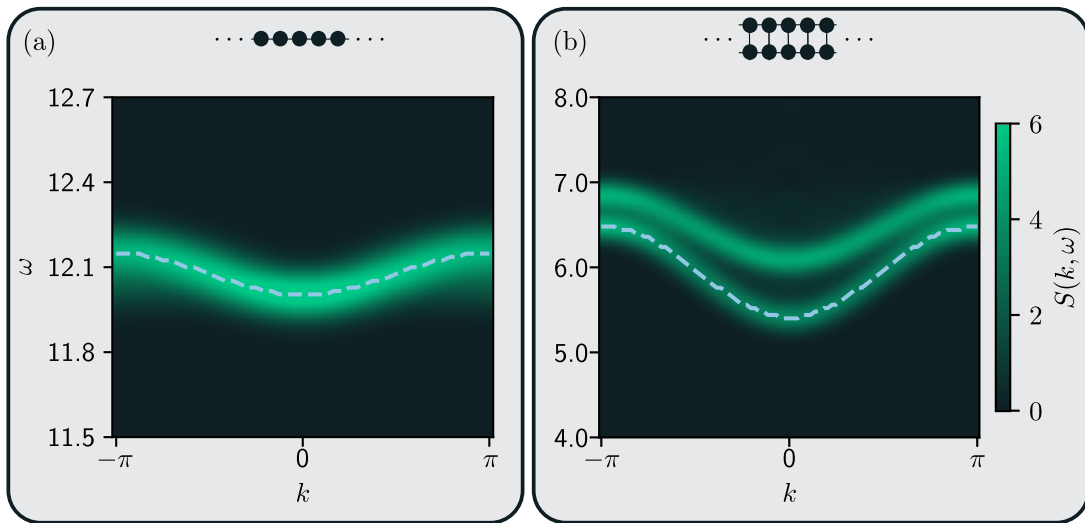


FIG. 4: The dynamical structure factor for the two *ferromagnetic* systems: (a) the TFIC with a longitudinal field with $h_x = 1$ and $h_z = 4$, and (b) the TFIL with $h_x = 1$, $h_z = 0$, and inter-chain coupling $\lambda = 1$. In both cases, dashed lines indicate the lowest energy level of the system.

Appendix C: Fourier Fitting Procedure

To extract dominant frequency components from the QPU data, we employ a Fourier fitting procedure based on the dominant spectral features observed in classical simulations. The fitting model is defined as

$$f(x) = (c_0 e^{-\gamma x} + c_1) \left(a_0 + \sum_{i=1}^N a_i \cos(\omega_i x) + b_i \sin(\omega_i x) \right), \quad (\text{C1})$$

where c_i , γ , a_i , and b_i are real-valued coefficients to be optimized, ω_i are the frequencies initialized using the dominant components identified from the classical spectrum, and γ is an exponential decay rate accounting for signal damping over time. We choose this Fourier form to isolate the dominant frequencies present in the QPU time traces and enable direct comparison with the classical results. The fitting minimizes the mean squared error (MSE) between the QPU data and the model, with all parameters — including amplitudes, frequencies, decay rate, and offset — allowed to vary unconstrained during optimization.

For each QPU dataset, we initialize the frequencies ω_i to those obtained classically, as this initialization consistently leads to the lowest loss without overfitting. We perform 20 independent optimization runs using the ADAM optimizer implemented in PyTorch [36, 43], each over 20,000 epochs. The number of epochs was chosen because the loss typically plateaus by this point, indicating convergence. Finally, the frequencies extracted from each run are averaged to yield robust estimates that mitigate the effects of statistical fluctuations, hardware noise, and optimizer variability.

Appendix D: QPU Hardware and Noise Analysis

In this section, we analyze the experimental results presented in Fig. 3 of the main text and compare them to the exact theoretical predictions. The experimental runs were carried out on our cloud-based commercial device Orion alpha operating at a shot rate of ~ 1 Hz. For each simulation, observables were measured at 100 distinct time steps, with 100 shots taken per time step. Additionally, each batch of 100 shots required the realization of a custom atomic register, which introduced an overhead. Taking all these factors into account, the total runtime for each complete simulation was approximately 4.5 hours. Multiple simulations were conducted with all yielding consistent performance across runs, which underscores the reliability of the observed trends.

Although the experimental data do not exactly match the classically obtainable results, the discrepancies are relatively minor and within acceptable bounds for the physics we aimed to capture in this work. Importantly, we are able to closely reproduce the QPU output using a detailed noise model. This model accounts for the various dominant sources of experimental imperfection, including SPAM, atomic position fluctuations resulting from finite trap widths, shot-to-shot variability in the Rabi frequency, a calibration-related shift in the detuning parameter, and dephasing noise; see Fig. 5. The noise model is implemented by sampling error parameters from experimentally motivated and testable distributions, followed by the execution of multiple Monte Carlo trajectories. The average over

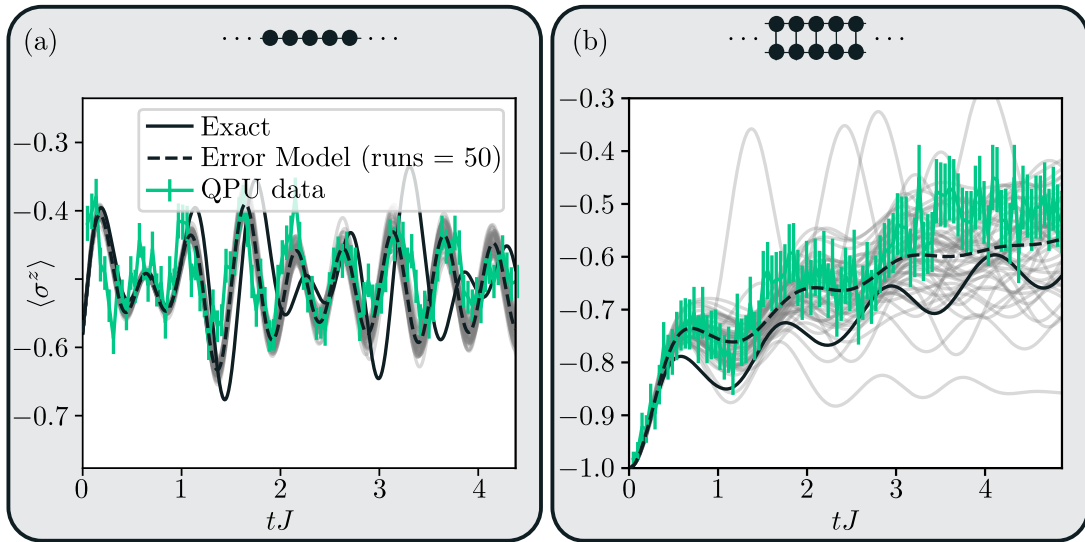


FIG. 5: Noise analysis of the QPU result presented in the main text. Here we show that by taking into consideration a experimentally realistic noise model we can recapture the results of the hardware. This model consists of SPAM, atomic position fluctuations, variability in the Rabi frequency, a shift in the detuning, and dephasing noise.

these trajectories provides an approximation of the error in the QPU [44]. These factors together provide a coherent explanation for the observed deviations and highlight the utility of noise-aware modeling in interpreting quantum hardware behavior.